Alkaline-based aqueous sodium-ion batteries for large-scale energy storage

Shizhang Qiao (s.qiao@adelaide.edu.au)
University of Adelaide https://orcid.org/0000-0002-4568-8422
Han Wu
The University of Adelaide
Junnan Hao
The University of Adelaide
Yunling Jiang
The University of Adelaide
Yiran Jiao
The University of Adelaide
Jiahao Liu
The University of Adelaide
Xin Xu
The University of Adelaide
Kenneth Davey
The University of Adelaide https://orcid.org/0000-0002-7623-9320
Chunsheng Wang
University of Maryland, College Park https://orcid.org/0000-0002-8626-6381

Article

Keywords:

Posted Date: April 13th, 2023

DOI: https://doi.org/10.21203/rs.3.rs-2783165/v1

Additional Declarations: Yes there is potential Competing Interest. H. Wu and S.-Z. Qiao have filed a PCT provisional patent covering materials and sodium aqueous battery application(s) described in this manuscript.

Version of Record: A version of this preprint was published at Nature Communications on January 17th, 2024. See the published version at https://doi.org/10.1038/s41467-024-44855-6.

Abstract

Aqueous sodium-ion batteries (ASIBs) are practically promising for large-scale energy storage, but their energy density and lifespan are hindered by water decomposition. Current strategies to enhance the water stability include using expensive fluorine-containing salts to create a solid electrolyte interface or adding potentially-flammable organic co-solvents in the electrolyte to reduce water activity. However, these methods have significantly increased cost and safety risk. Shifting electrolytes from near neutrality to alkalinity can fundamentally suppress hydrogen evolution, but trigger oxygen evolution and cathode dissolution. Here, we present an alkaline-type ASIB with Mn-based Prussian blue analogue cathode, which exhibits a record lifespan of 13,000 cycles at 10 C together with high energy density of 90 Wh kg−1 at 0.5 C. This is achieved by building a nickel/carbon layer to induce a H3O+-rich local environment near the cathode surface, thereby suppressing oxygen evolution and cathode dissolution. Simultaneously, Ni atoms can be in-situ embedded into the cathode to enable its durability. At an industry-level mass loading > 30 mg cm−1, the pouch cell exhibits excellent stability with a capacity retention of ~ 100% following 200 cycles at 300 mA g−1, outperforming previously reported aqueous batteries.

Full Text

The growing demand for large-scale energy storage has boosted the development of batteries that prioritize safety, low environmental impact, and cost-effectiveness[1-3]. On account of abundant sodium and the compatibility with commercial industrial systems[4], aqueous sodium-ion batteries (ASIBs) are practically promising for affordable, sustainable, and safe large-scale energy storage. However, their energy density and cycling stability are limited due to the narrow electrochemical stability window of 1.23 V for water. Additionally, the accumulation of flammable hydrogen (H_2) from water decomposition during cycling compromises battery safety and restricts the development of ASIBs. One common strategy for improving the performance of aqueous batteries is to use expensive fluorine-containing salts to create a solid-electrolyte interphase (SEI)[5] that can suppress the hydrogen evolution reaction (HER) and increase the electrochemical window of the electrolyte. However, the high solubility of SEI components such as LiF, NaF, and Na_2CO_3 limits its durability[6]. Moreover, the high cost of fluorine-containing salts significantly compromises the cost-effectiveness of aqueous batteries. Another approach involves using co-solvents[7], including polymers, to improve the water stability of the electrolyte. Unfortunately, these strategies significantly increase the viscosity of the electrolyte, making it challenging to match with high loading electrodes for commercial applications. The organic co-solvents' potential flammability also compromises the safety of aqueous batteries. Therefore, developing alternative strategies to enhance the water stability of aqueous batteries while maintaining their cost-effectiveness and safety is a critical research priority.

Compared to conventional aqueous electrolytes with a pH close to 7, alkaline electrolytes offer thermodynamic suppression of HER on the anode based on the Pourbaix diagram for water[8]. Whereas shifting the electrolyte from near neutrality to alkalinity aggravates the oxygen evolution reaction (OER)

on the cathode[9]. Furthermore, the high concentration of OH^- in electrolytes limits the choice of cathodes as it interacts with transition metal-based electrodes, leading to the deterioration of electrode structures, especially for Prussian blue analogues (PBAs) cathodes[10]. As the commonly used Mn-based PBAs, they have been widely studied in traditional aqueous batteries benefiting from advantages of non-toxicity, low cost, and high energy density[5-7]. Nevertheless, their potential use in alkaline electrolytes is constrained due to the strong Jahn-Teller effects in the redox couples of Mn^{2+}/Mn^{3+} as well as the dissolution of Fe[11]. Consequently, PBA-based alkaline ASIBs have not been reported to date.

Here, we report a hydrogen-free alkaline ASIB based on a Mn-based PBA cathode ($Na_2MnFe(CN)_6$, NMF), $NaTi_2(PO_4)_3$ (NTP) anode, and an affordable alkaline electrolyte of fluorine-free sodium perchlorate ($NaClO_4$) whose price is much cheaper than commonly-used sodium triflate and sodium bis(trifluoromethylsulfonyl)imide in highly concentrated electrolytes. As illustrated in **Fig. 1a**, the alkaline electrolyte effectively suppresses HER at the anode. Moreover, by coating a commercially available nickel/carbon (Ni/C) nanoparticle-based layer on the NMF cathode, a H_3O^+-rich local environment forms near the cathode surface. This H_3O^+-rich local environment results from the irreversible formation of $Ni(OH)_2$ and reversible $Ni(OH)_2$/NiOOH redox (confirmed by *in-situ* Attenuated Total Reflectance Infrared (ATR-IR), Raman and *Operando* synchrotron X-ray powder diffraction, XRPD), which significantly reduces OER and electrode dissolution. Additionally, partial Ni atoms in the coating are *in-situ* embedded in the cathode to stabilize the NMF structure in alkaline media, as confirmed by *operando* Raman and high-angle annular dark-field scanning transmission electron microscopy (HAADF-STEM).

Electrochemical performance of alkaline NMF/NTP coin cells

At first, the prepared NMF, NTP, and the commercial Ni/C powders were studied by X-ray diffraction (XRD, **Supplementary Figs. 1-3**), indicating their good crystallinity for further applications in batteries. Then, the impact of salt concentration in electrolytes on HER was investigated by *in-situ* differential electrochemical mass spectrometry (DEMS) in $NaClO_4$ electrolytes with selected salt concentrations. Results show that, without forming a reliable SEI, increasing the electrolyte concentration cannot change the onset potential of HER (**Supplementary Fig. 4**).

Notably, increasing the alkalinity of electrolyte suppresses HER (**Supplementary Figs. 5a-c**), which contributes to a better cycling stability of NTP anode (**Supplementary Figs. 6a-c)**. However, the increased alkalinity of electrolyte propels OER (**Supplementary Fig. 5d**) and also increases the dissolution rate of Fe and Mn elements[12] of the NMF cathode, leading to the poor cycling stability even at a water-stable voltage range of 0-1.0 V (**Supplementary Figs. 6d-e** and **h**). In comparison, after coating Ni/C layer on the NMF electrode (thickness: *ca*. 1 μm, **Supplementary Fig. 7**), its cycling stability is significantly enhanced (**Supplementary Figs. 6f)**, as confirmed by the unchanged electrolyte colour (**Supplementary Figs. 6i**) as well as the suppressed Fe dissolving concentration in the electrolyte verified by results of inductively coupled plasma mass spectrometry (ICP-MS) (**Supplementary Fig. 8**).

The performance of NMF/NTP full cells using neutral electrolyte or alkaline electrolyte with/without Ni/C coating, was evaluated in a wide charging voltage range of 0.5 to 2.2 V. The NMF/NTP full cell with Ni/C coating exhibits a highly boosted rate performance and higher average discharge voltage than those without Ni/C coating, contributing to the fast-charge ability and high energy density of the battery (**Supplementary Figs. 9a-b**). **Fig. 1b** compares the cycling performance of NMF/NTP batteries under three different conditions at 1 C. Batteries without Ni/C coating in both neutral and alkaline electrolytes show a rapid capacity decay with capacity retention of < 60% following 200 cycles, whereas the alkaline-based battery with Ni/C coating exhibits a higher retention of ~ 100%. Furthermore, the electrolyte exhibits a lower freezing point in comparison to previously reported highly concentrated electrolytes[5, 11]„ allowing the battery to function effectively at low temperatures. (**Supplementary Fig. 10**). Consequently, the battery with Ni/C coating displays a capacity retention of 91.3% after 200 cycles at 0.5 C under −30 °C (**Fig. 1c**). Importantly, this full cell features a record lifespan of > 13,000 cycles with a high capacity retention of 74.3% at 10 C (**Fig. 1d)**, surpassing mostly previously reported aqueous batteries[13].

Pouch cell's performance and comparison

To meet commercial requirements for large-scale energy storage, a Ni/C coated NMF//alkaline electrolyte//NTP pouch cell was assembled with the electrode loading of *ca*. 20 mg cm^{-2}. This pouch cell exhibits a high capacity retention of 85% following 1,000 cycles at 500 mA g^{-1} (**Fig. 2a**). Additionally, the mass loading of single electrode can be further increased to the industry level of > 30 mg cm^{-2} benefiting from the low viscosity of the alkaline electrolyte (6.0 mPa s, **Supplementary Table 1**). Under such high loading, NMF/NTP pouch cell shows stable cycling life with a capacity retention of ~ 100% within 200 cycles at 300 mA g^{-1} (**Fig. 2b**). This large-size pouch cell also exhibits an ultra-high stability under 'harsh' conditions of cutting and immersion in water (**Supplementary Videos 1-2**, **Supplementary Figs. 11a-c** and **Fig. 2c**). In addition, the cut pouch cell can continuously power a humidity clock in water for > 20 h (**Supplementary Video 3** and **Fig. 2d**). This confirms that the battery is resistant to electrolyte leakage and can withstand significant damage in high-humidity environments. As a result, the battery offers high safety for practical applications in energy storage and underwater electrical equipment.

Significantly, in addition to high safety, our battery design reduces the cost of manufacture and fabrication *via* hiring low-cost fluorine-free salt. Compared to other electrolytes for reported aqueous Li/Na/K ion batteries with an energy density of > 80 Wh kg^{-1} (based on total mass of anode and cathode), our electrolyte has a significantly lower unit-cost (the detailed comparison displays in **Supplementary Fig. 12** and **Supplementary Table 2**), which guarantees the actual application of alkaline-based batteries. Furthermore, our batteries can achieve a high cycling stability and discharge capacity under ultra-low positive/negative capacity ratio of 1.06. Under such a low capacity ratio and 0.5 C charging rate, a greatest energy density amongst ASIBs (90 Wh kg^{-1}) can be obtained (**Fig. 2e** and **Supplementary Table 3**). Compared to reported electrochemical battery storage devices, our battery system possesses significant advantages including, use of abundant elements (such as Fe, Mn, and Ti), high safety (high toleration to high humidity environment), environment friendliness (non-poisonous

electrolyte), and a record lifespan (**Fig. 2f** and **Supplementary Table 4**). Although its energy density is slightly lower than that of Li-ion and nickel-metal-hydride (Ni-MH) batteries, its cost-efficacy and safety, namely key requirements for large-scale energy storage, are superior.

The origin of H_3O^+-rich local environment

To determine underlying factors for the high performance of the alkaline ASIB, the interface structure with Ni/C coating was assessed *viain-situ* ATR-IR spectroscopy. The carbon coating was taken as a 'control' to eliminate any influences of carbon support. For the electrode modified by pure carbon, the spectra exhibit no apparent change even after being charged to 1.3 V (*vs.* Ag/AgCl), evidencing that the carbon and binder do not change microenvironment of the cathode surface (**Fig. 3a,** the function of carbon in Ni/C coating is discussed in **Supplementary Text S1** and **Supplementary Fig. 13**). In contrast, with Ni/C modification, new peaks at 1,798 and 2,032 cm^{-1} appear when the potential is > 0.6 V, attributed to two asymmetric O-H stretching modes of H_3O^+ ($\nu^{a^1}_{H_3O^+}$ and $\nu^{a^2}_{H_3O^+}$). Peaks of the resonance state for the asymmetric O-H stretching modes in H_3O^+ ($\nu^{a^2,r+u}_{H_3O^+}$) at 2,223 cm^{-1} and the umbrella vibration for H_3O^+ ($\nu^{u}_{H_3O^+}$) at 1,230 cm^{-1} are also visible[14], confirming the H_3O^+ accumulation on the electrode surface induced by Ni nanoparticles. This accumulation of H_3O^+ (D_3O^+) was further confirmed *via in-situ* Raman when using D_2O as a solvent, evidenced by the appearance of a new peak for D_3O^+ and HD_2O^+ with increasing the applied working potential[15] (**Supplementary Fig. 14a**). *Operando* DEMS was employed to determine the water decomposition in this alkaline battery system during battery cycling. The battery without Ni/C coating exhibits HER and OER concurrently at a low positive/negative capacity ratio in the neutral electrolyte (**Supplementary Fig. 14b**). However, after coating Ni/C on the NMF cathode in alkaline electrolyte, both HER and OER become inconspicuous, except for trace O_2 at the first cycle before activating the surface coating (**Fig. 3b**). It can be concluded that the H_3O^+-rich local environment induced by Ni/C protective layer suppresses the deteriorative OER in the alkaline electrolyte, while the alkaline electrolyte effectively retards HER.

The H^+ accumulation mechanism on the electrode surface with Ni/C is illustrated in **Fig. 3c**. The H_3O^+ comes from water dissociation, inequivalent adsorption ability of H^+ and OH^- on Ni, together with a reversible transformation between $Ni(OH)_2$ and NiOOH. Ni nanoparticles promote water dissociation, resulting in the production of H^+ and OH^- around this coating[16]. The OH^- from bulk alkaline electrolyte and water dissociation on the surface of Ni can be confined due to the strong interaction between Ni and

OH^-, as evidenced by density functional theory (DFT) simulations (**Supplementary Table 5**). As the applied potential on Ni increases, the interaction between Ni and H^+ becomes weaker whilst the interaction between Ni and OH^- remains stable, evidencing that H_3O^+ is more likely to be generated at high voltages, which is confirmed by ATR-IR and Raman spectra mentioned before. Moreover, Ni is oxidized to $Ni(OH)_2$ at higher voltages to bond with OH^-. Additional H^+ is generated when $Ni(OH)_2$ is oxidized to NiOOH, as confirmed by XRPD and soft X-ray absorption spectra (XAS, **Supplementary Figs. 15-16** and **Supplementary discussion Text S2**). Thereby, H^+ bonds with nearby water molecules rather than Ni nanoparticles to form H_3O^+. These H_3O^+ ions exposed to bulk alkaline electrolyte are readily neutralized by excess OH^-. In contrast, because of physical blocking of the coating, abundant H_3O^+ ions underneath the coating accumulate, leading to a H_3O^+-rich local environment on the cathode surface that suppresses OER during battery operation.

Ni-substituted process

Besides the increased OER, the improved alkalinity of electrolyte also compromises the cycling stability of PBA-based cathode material (without Ni/C coating). During charging/discharging process, the lattice constants of NMF changes in limited ranges accompanied by redox reactions of Mn, which causes collapse of Fe–CN–Mn bridges and vacancy generation[17], as confirmed by gradually missing of the first discharge plateau (Figs. 4a-b). The dissolution of NMF is aggravated in alkaline electrolyte (**Supplementary Figs. 17-18**), which further decreases the stability of NMF cathode[12]. In contrast, the first discharge plateau for NMF/NTP cell and the structure of NMF cathode exhibit ultra-high stability after Ni/C coating even after 80 cycles (**Fig. 4c**). The stable discharge plateau for NMF/NTP after coating is mainly due to the *in-situ* substitution of Ni atoms to balance 'tiny' structural disturbances caused by redox reactions in Mn sites[10, 18, 19] (**Fig. 4d**).

This hypothesis is confirmed by *operando* Raman spectra of Ni/C coated NMF cathodes cycled in the alkaline electrolyte (**Fig. 4e**). Peaks in the range of 2,050 to 2,200 cm^{-1} are assigned to cyano (CN) groups, evidencing that CN^- groups bond with transition-metal ions with diverse valence states. Prior to cycling, two peaks at 2,089 and 2,124 cm^{-1} are visible, corresponding to Fe^{2+}–CN–Mn^{2+} and Fe^{2+}–CN–Mn^{3+} vibrations, respectively[20]. After charging to 1.89 V, both peaks disappear, evidencing transformation of Fe^{2+} to Fe^{3+} and Mn^{2+} to Mn^{3+}. More importantly, after charging to 2.2 V, a new 'weak' peak appears at 2,195 cm^{-1} corresponding to Fe^{3+}–CN–Ni^{2+} [21]. This finding confirms the introduction of Ni atom in NMF particle following transformation of Mn^{2+} to Mn^{3+}. After discharging to 0.5 V, peaks for Fe^{2+}–CN–Mn^{2+} and Fe^{2+}–CN–Mn^{3+} shift to 2,092 and 2128 cm^{-1} and a new peak appears at 2,164 cm^{-1} that is assigned to Fe^{2+}–CN–Ni^{2+} [21]. The introduction of Ni is also proved by the HAADF-STEM and energy-dispersive spectroscopy (EDS) mapping (**Fig. 4f**). Additionally, the EDS line-scan spectra for a single NMF particle confirms that Ni atoms are introduced into the edge of particles to suppress dissolution of inner Mn atoms (**Fig. 4g**). The EDS mappings for NMF cathode with Ni/C coating following 1^{st}, 5^{th} and 20^{th} cycles (**Supplementary Table 6** and **Supplementary Fig. 19**) evidence that the content of

Ni in NMF particles is stable after the first cycle, confirming that the introduction of Ni into NMF cathode reaches an equilibrium in the first cycle to guarantee a long-term stability of the cathode.

This structure stability of NMF cathode achieved by the introduction of 'inert' Ni atoms in alkaline electrolyte is confirmed *via* XRPD patterns during charge/discharge. The structural evolutions of NMF structure happened at a high voltage range over 1.7 V, ascribing to the Mn^{2+} to Mn^{3+} (**Fig. 5a**). **Fig. 5b** shows the 2D contour map of NMF reflection. The highly reversible structure evolution during charge and discharge process can be easily observed. Further, the Rietveld refinements of NMF with/without Ni/C coating after 1st cycle show that both electrodes exhibit cubic phases with Fm-3m space group and a = b = c (**Figs. 5c-d** and **Supplementary Table 7**), however, the lattice parameters for Ni/C coated NMF (5.28161 Å) are greater than that for uncoated NMF (5.26358 Å). This finding is attributed to the introduction of Ni in Ni/C coated NMF upon cycling. An increased a (b, c) contributes to a boosted rate performance for the cathode, which is consistent with our results (**Supplementary Fig. 9a)**. Importantly, compared to the deteriorated structure of uncoated NMF after 1st and 3rd cycle (**Fig. 5e)**, the overlapping patterns for Ni/C coated NMF following 1st and 3rd cycle confirm the excellent stability of NMF and that Ni introduction occurs at 1st cycle, because otherwise, continuous Ni introduction will change the XRPD pattern (**Fig. 5f**).

To assess the possible universality of the new electrode modification strategy in alkaline batteries, the Co/C nanoparticle was employed to build the cathode coating as well. Similar to Ni nanoparticle, Co can be oxidized to $Co(OH)_2$ in alkaline media and, it possesses reversible redox pair of $Co(OH)_2$/CoOOH, together with ability to *in-situ* substitute the Mn atom. As a result, the good stability of battery with Co/C coating is achieved (**Supplementary Fig. 20**). This discovery provides evidence for the universality of creating H_3O^+-rich cathode surfaces and *in-situ* optimizing the NMF structure by building metal nanoparticle coating to enhance the performance of alkaline ASIBs.

Conclusion

A new aqueous battery system, differing from traditional ASIBs based on near neutral electrolyte, is presented with a fluorine-free alkaline electrolyte to suppress H_2 evolution on the anode and a Ni/C coating to alleviate both O_2 evolution and electrode dissolution on the cathode. This system achieves long cycling stability (13,000 cycles) and high energy density (90 Wh kg^{-1}) in the alkaline electrolyte through the Ni/C coating induced H_3O^+-rich local environment and *in-situ* electrode Ni modification. Remarkably, the cost of this alkaline electrolyte is *ca.* 25 times cheaper than commonly used highly concentrated fluorine-containing electrolytes. The pouch cell, assembled with an ultra-high electrode loading of > 30 mg cm^{-2}, maintains a capacity retention of ~100% following 200 cycles, while demonstrating excellent safety even after being cut and immersed in water. This aqueous alkaline battery design strategy shows the universality by extending to Co/C and exhibits the prospect for achieving high energy density by coupling with other lower redox potential anodes (**Supplementary Fig. 21**). Importantly,

this strategy can be expanded flexibly to various aqueous batteries and will boost the large-scale application of aqueous batteries.

Methods

Materials

The $Na_2MnFe(CN)_6$ (NMF) cathode and $NaTi_2(PO_4)_3$ (NTP)/C anode were synthesized based on reported methods[22]. The Nafion-Na was prepared through the neutralization reaction of 10 mL Nafion (purchased from *DuPont*, D520, 5 wt%) with 0.01 M NaOH solution drop-by-drop. Product was collected following removal of the solvent at 60 °C. 20% Ni/C was purchased from *Fuel Cell Stor*e.

Electrode preparation

The NMF electrode was prepared *via* mechanically mixing 80wt.% NMF, 10wt.% Super-P and 10wt.% polytetrafluoroethylene (PTFE) binder dispersed in ethanol solvent (AR). The mixture was pressed on a Ti-mesh at a pressure of 6 MPa and dried at 70 °C for 2 h in a vacuum oven. The NTP electrode was prepared by the same procedure as for NMF electrode using 80 wt.% NTP/C (~ 5% C), 10 wt.% Super-P and 10wt.% PTFE. The mass loading for electrodes was *ca.* 10 mg cm^{-2}. The mass ratio of anode and cathode in coin cell was ~ 1/1.06. The electrodes in the pouch cell were prepared with the same method. The mass ratio of anode and cathode in pouch cell was ~ 1/1.15. The specific capacity computation was based on the mass of cathode.

Electrolyte preparation

41.6 g $NaClO_4$ was dissolved in 20 mL water to obtain near neutral electrolyte. Alkaline electrolytes were obtained *via* addition of, respectively, 0.1, 0.2, 0.4 and 0.8 mL 1 M NaOH solution into 30 mL of neutral electrolyte.

Coating preparation

The coating was prepared as follows: 0.1 g Nafion-Na was dissolved in mixed solution of 0.45 g N, N-Dimethylformamide and 0.45 g isopropanol at 60 °C. 0.025 g Ni/C was, magnetic stirred for 0.5 h, and ultrasounded for 0.5 h. Procedures were replicated three times to give an even mixture. 10 μL cm^{-2} solution was sprayed on the surface of cathode discs. Following removal of the solvent at room temperature (RT) (~ 25 °C) in N_2-filled glove-box under vacuum over 24 h, the electrode discs were coated homogenously.

Electrochemical measurement

LSV was measured in a three-electrode cell at a scanning speed of 1 mV s^{-1}. In the three-electrode cell, glass carbon was used as the working electrode, Ti as the counter electrode, and an Ag/AgCl electrode as the reference electrode, respectively. The three-electrode cell for testing cathodes was assembled with

NMF composite (20 mg cm^{-2}) as the working electrode, activated carbon as the counter electrode, and Ag/AgCl as reference electrode. The three-electrode cell for testing anodes was assembled with the NTP composite (19 mg cm^{-2}) as the working electrode, activated carbon as the counter electrode, and Ag/AgCl as reference electrode.

Characterizations

In situ Attenuated Total Reflectance Infrared (ATR-IR) spectroscopy was performed with a Thermo-Fisher Nicolet iS20 equipped with a liquid, nitrogen-cooled HgCdTe (MCT) detector using a VeeMax III ATR accessory (Pike Technologies). A germanium prism (60°, Pike Technologies) was mounted in a PIKE electrochemical three-electrode cell with an Ag/AgCl reference electrode (Pine Research) and a Pt- wire counter electrode. To obviate any significant influences from the electrolyte, nanocarbon particles and polymer support, the spectrum without applying voltage was taken as a background. Tests were undertaken using a three-electrode cell with Pt as the counter electrode and Ag/AgCl as reference. DEMS was used to monitor volatile gases of H_2 and O_2 produced during battery operation at RT (Hidden HPR40). *In-situ* Raman spectroscopy for the Ni/C coating layer was determined using a confocal Raman microscope (Horiba LabRAM HR Evolution) with a 60X (1.0 N.A) water-immersion objective (Olympus). Laser wavelength was 532 nm. A screen-printed electrode (Pine, RRPE1002C) was used as the electrode for tests with a CHI 760E work-station. The working electrode was coated with Au *via* magnetron sputtering. 15 mL, 17 m (molar/$kg_{solvent}$) $NaClO_4$ in D_2O with addition of 0.2 mL 1 M (molar/L) NaOH in D_2O was used as the isotopically labelled electrolyte. XRD patterns were determined using a Bruker-AXS Micro-diffractometer (D8 ADVANCE) with Cu-Kα1 radiation (λ = 1.5405 Å). HAADF-STEM, EDS mapping and line-scan spectra were used to confirm existence of Ni in cycled NMF particles (FEI Titan Themis 80-200). A cross-section of coated NMF cathode was determined *via* field emission (FE) focused ion-beam (FIB, Helios NanoLab 600), and data collected by SEM and EDS with a field emission scanning electron microscope (FEI Quanta 450). ICP-MS was collected using Agilent 8900. Soft XAS was tested in the Australian Synchrotron. *Operando* synchrotron X-ray powder diffraction was conducted in the Australian Synchrotron and, the battery tested using Neware battery test system (CT-3008-5V1mA-164, Shenzhen, China). Home-made 2032-coin cells were used for data collection. Both sides of the cell cases were ‘punched’ with a central, 5 mm diameter hole, and sealed with Kapton film as the beam entrance. XRD data from the synchrotron were refined *via* the Rietveld method using GSAS II software.

DFT simulation

Density functional theory (DFT) computations were performed by Vienna *Ab Initio* Simulation Package (VASP.5.4.4)[23, 24]. Generalized gradient approximation (GGA) with Perdew-Burke-Ernzerhof (PBE) function was used for describing the exchange-correlation potential[25, 26]. Ni(111) and Ni(200) slabs were modeled using 33 unit cells with four layers, whilst the two topmost layers were allowed to fully relax until the convergence criterion of 10^{-5} eV for energy and 0.02 eV/Å for final forces on atoms, whilst other layers were fixed. Energy cut-off was set as 600 eV. DFT-D3 correction method was used for describing the van der Waals interaction. A (33) Monkhorst-Pack k-point grid mesh was used. An implicit solvent model was

used to simulate the solvent environment using Polarizable Continuum Model (PCM) provided by VASPSOL[27, 28], where ε_r = 80 for the water system.

For the adsorption energy (ΔG_{ads}) for *H_2O, the reference state was set based on the liquid phase computed from, namely: $G_{H_2O(l)} = G_{H_2O(g)} + RT \times \ln(p/p_0)$, and; $G_{H_2O(g)}$ determined *via* DFT computation. The adsorption energy for other absorbents, including OH and H, was computed from: $G_{OH^-} = G_{H_2O(l)} - G_{H^+}$ and; $G_{H^+} = 1/2G_{H_2} - k_B T \ln 10 \times pH$, with pH = 12 used throughout.

ΔG_{ads} for a charge-neutral surface (ΔG_{ads}^{cnm}) was computed from:

$$\Delta G_{ads}^{cnm} = G_1 - G_0 - G_{H^+} + |e|U \quad (1)$$

where G_1 and G_0 denote, respectively, free energy for Ni surface with and without species adsorption and U is applied voltage *vs*. SHE model. The superscript cnm represents charge-neutral conditions. For the charge effect from applied voltage, an alternative constant-potential DFT (CP-DFT) can be reliably used. With this, the Fermi energy for the catalyst prior to ($E_{Fermi}^{Q_0}$) and following adsorption ($E_{Fermi}^{Q_1}$) using electron energy (μ_e) is as follows[29]:

$$E_{Fermi}^{Q_0} = E_{Fermi}^{Q_1} = \mu_e \quad (2)$$

where μ_e is determined from applied voltage, therefore is U dependent.

To satisfy Equation (1) a manipulation of surface charge prior to and following adsorption (Q_0 and Q_1) is needed to maintain a specific Fermi energy. For this, ΔG_{ads} under CP-DFT () can be rewritten as[30]:

$$\Delta G_{ads}^{cp} = G_1^{Q_1} - G_0^{Q_0} - G_{H^+} - (Q_0 - Q_1) \times \mu_e \quad (3)$$

where $G_1^{Q_1}$ and $G_0^{Q_0}$ are free energy obtained with CP-DFT. The catalyst is embedded in the electrolyte with a Poisson-Boltzmann model implemented *via* VASPSOL that balances the added charge by counter ions in solution and therefore obviates the using of a charged unit cell.

Declarations

Acknowledgements: The authors gratefully acknowledge financial support from the Australian Research Council (DP220102596, LP210301397 and DE230100471). DFT computations were undertaken with the assistance of resources and services from the National Computational Infrastructure (NCI) and Phoenix High Performance Computing, supported by the Australian Government and, The University of Adelaide. This research was undertaken on the XAS and Soft X-ray beamlines at the Australian Synchrotron, part of ANSTO. The authors acknowledge Dr. Ashley for assistance with TEM testing, and TEM measurements were undertaken at Adelaide Microscopy, the Centre for Advanced Microscopy and Microanalysis. The authors thank Tingting Liu from the Qingdao Institute of Bioenergy and Bioprocess Technology for the assistance with of DEMS testing.

Author contributions: S.-Z. Qiao conceived and supervised the project. H. Wu and J. Hao designed research, conducted characterizations and electrochemical measurement. H. Wu, S.-Z. Qiao, K. Davey, C. Wang and J. Hao analysed data and wrote manuscript. H. Wu, J. Hao, Y. Jiang, J. Liu and X. Xu conducted characterizations of materials. Y. Jiao conducted DFT computations. H. Wu and J. Hao contribute equally to this work. All authors agreed on the manuscript and approved submission.

Competing interests: H. Wu and S.-Z. Qiao have filed a PCT provisional patent covering materials and sodium aqueous battery application(s) described in this manuscript.

References

1. Borodin, O. et al., Uncharted waters: Super-concentrated electrolytes, *Joule*, **4**, 69-100 (2020).
2. Fan, X.L. et al., Non-flammable electrolyte enables Li-metal batteries with aggressive cathode chemistries, *Nat. Nanotechnol.*, **13**, 715-722 (2018).
3. Liu, T.C. et al., Understanding Co roles towards developing Co-free Ni-rich cathodes for rechargeable batteries, *Nat. Energy*, **6**, 277-286 (2021).
4. Abraham, K.M., How comparable are sodium-ion batteries to lithium-ion counterparts?, *ACS Energy Lett.*, **5**, 3544-3547 (2020).

5. Suo, L.M. et al., "Water-in-salt" electrolyte enables high-voltage aqueous lithium-ion chemistries, *Science*, **350**, 938-943 (2015).
6. Droguet, L. et al., Water-in-salt electrolyte (WiSE) for aqueous batteries: a long way to practicality, *Adv. Energy Mater.*, **10**, 2002440 (2020).
7. Chua, R. et al., Hydrogen-bonding interactions in hybrid aqueous/nonaqueous electrolytes enable low-cost and long-ifespan sodium-ion storage, *ACS Appl. Mater. Interfaces*, **12**, 22862-22872 (2020).
8. Zhu, Y.-h. et al., Decoupled aqueous batteries using pH-decoupling electrolytes, *Nature Reviews Chemistry*, **6**, 505-517 (2022).
9. Kim, H. et al., Aqueous rechargeable Li and Na ion batteries, *Chem. Rev.*, **114**, 11788-11827 (2014).
10. Lamprecht, X. et al., Electrolyte effects on the stabilization of prussian blue analogue electrodes in aqueous sodium-ion batteries, *ACS Appl. Mater. Interfaces*, **14**, 3515-3525 (2022).
11. Jiang, L.W. et al., Building aqueous K-ion batteries for energy storage, *Nat. Energy*, **4**, 495-503 (2019).
12. Stilwell, D.E. et al., Electrochemical studies of the factors influencing the cycle stability of prussian blue films, *J. Appl. Electrochem.*, **22**, 325-331 (1992).
13. Nian, Q.S. et al., Issues and opportunities on low-temperature aqueous batteries, *Chem. Eng. J.*, **423**, 10 (2021).
14. Zhan, C. et al., Dissolution, migration, and deposition of transition metal ions in Li-ion batteries exemplified by Mn-based cathodes - a critical review, *Energy Environ. Sci.*, **11**, 243-257 (2018).
15. Wang, X.S. et al., Anomalous hydrogen evolution behavior in high-pH environment induced by locally generated hydronium ions, *Nat. Commun.*, **10**, 8 (2019).
16. Hundt, P.M. et al., Vibrationally promoted dissociation of water on Ni(111), *Science*, **344**, 504-507 (2014).
17. Ge, J.M. et al., Surface-substituted prussian blue analogue cathode for sustainable potassium-ion batteries, *Nat. Sustain.*, **5**, 225-234 (2022).
18. Yang, D.Z. et al., Structure optimization of prussian blue analogue cathode materials for advanced sodium ion batteries, *Chem. Commun.*, **50**, 13377-13380 (2014).
19. Zhan, C. et al., Dissolution, migration, and deposition of transition metal ions in Li-ion batteries exemplified by Mn-based cathodes–a critical review, *Energy Environ. Sci.*, **11**, 243-257 (2018).
20. Asahara, A. et al., Growth dynamics of photoinduced phase domain in cyano-complex studied by boundary sensitive Raman spectroscopy, *Acta Phys. Pol. A*, **121**, 375-378 (2012).
21. You, Y. et al., A zero-strain insertion cathode material of nickel ferricyanide for sodium-ion batteries, *J. Mater. Chem. A*, **1**, 14061-14065 (2013).
22. Han, J. et al., Fluorine-free water-in-salt electrolyte for green and low-cost aqueous sodium-ion batteries, *Chemsuschem*, **11**, 3704-3707 (2018).
23. Kresse, G. & Furthmüller, J., Efficiency of ab-initio total energy calculations for metals and semiconductors using a plane-wave basis set, *Comput. Mater. Sci.*, **6**, 15-50 (1996).

24. Kresse, G. & Furthmüller, J., Efficient iterative schemes for ab initio total-energy calculations using a plane-wave basis set, *Phys. Rev. B*, **54**, 11169 (1996).
25. Perdew, J.P. et al., Generalized gradient approximation made simple, *Phys. Rev. Lett.*, **77**, 3865 (1996).
26. Kresse, G. & Joubert, D., From ultrasoft pseudopotentials to the projector augmented-wave method, *Phys. Rev. B*, **59**, 1758 (1999).
27. Letchworth-Weaver, K. & Arias, T.A., Joint density functional theory of the electrode-electrolyte interface: Application to fixed electrode potentials, interfacial capacitances, and potentials of zero charge, *Phys. Rev. B*, **86**, (2012).
28. Mathew, K. et al., Implicit solvation model for density-functional study of nanocrystal surfaces and reaction pathways, *J. Chem. Phys.*, **140**, (2014).
29. Garza, A.J. et al., Mechanism of CO_2 reduction at copper surfaces: Pathways to C-2 products, *ACS Catal.*, **8**, 1490-1499 (2018).
30. Kim, D. et al., Substantial impact of charge on electrochemical reactions of two dimensional materials, *J. Am. Chem. Soc.*, **140**, 9127-9131 (2018).

Figures

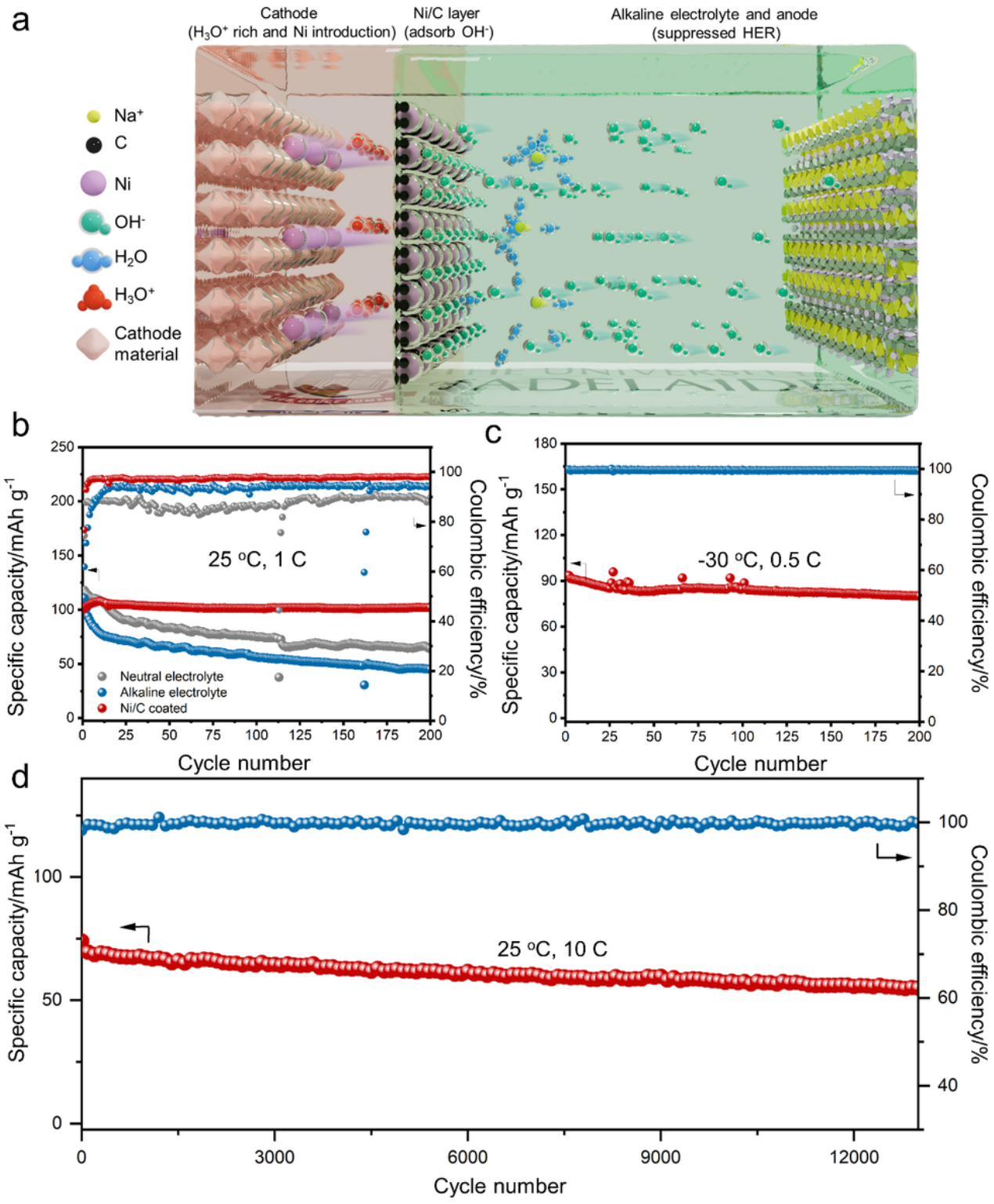

Figure 1

Electrochemical performance of NMF/NTP coin cells in the range of 0.5 to 2.2 V. a, Design concept for the alkaline aqueous battery. b, Cycling performance for three cells at 1 C. c, Cycling performance for NMF/NTP cell with Ni/C coating at 0.5 C at a low temperature of −30 °C. d, Long-term cycling stability for NMF/NTP full cell with Ni/C coating at 10 C, 1 C = 118 mA g^{-1}, based on NMF.

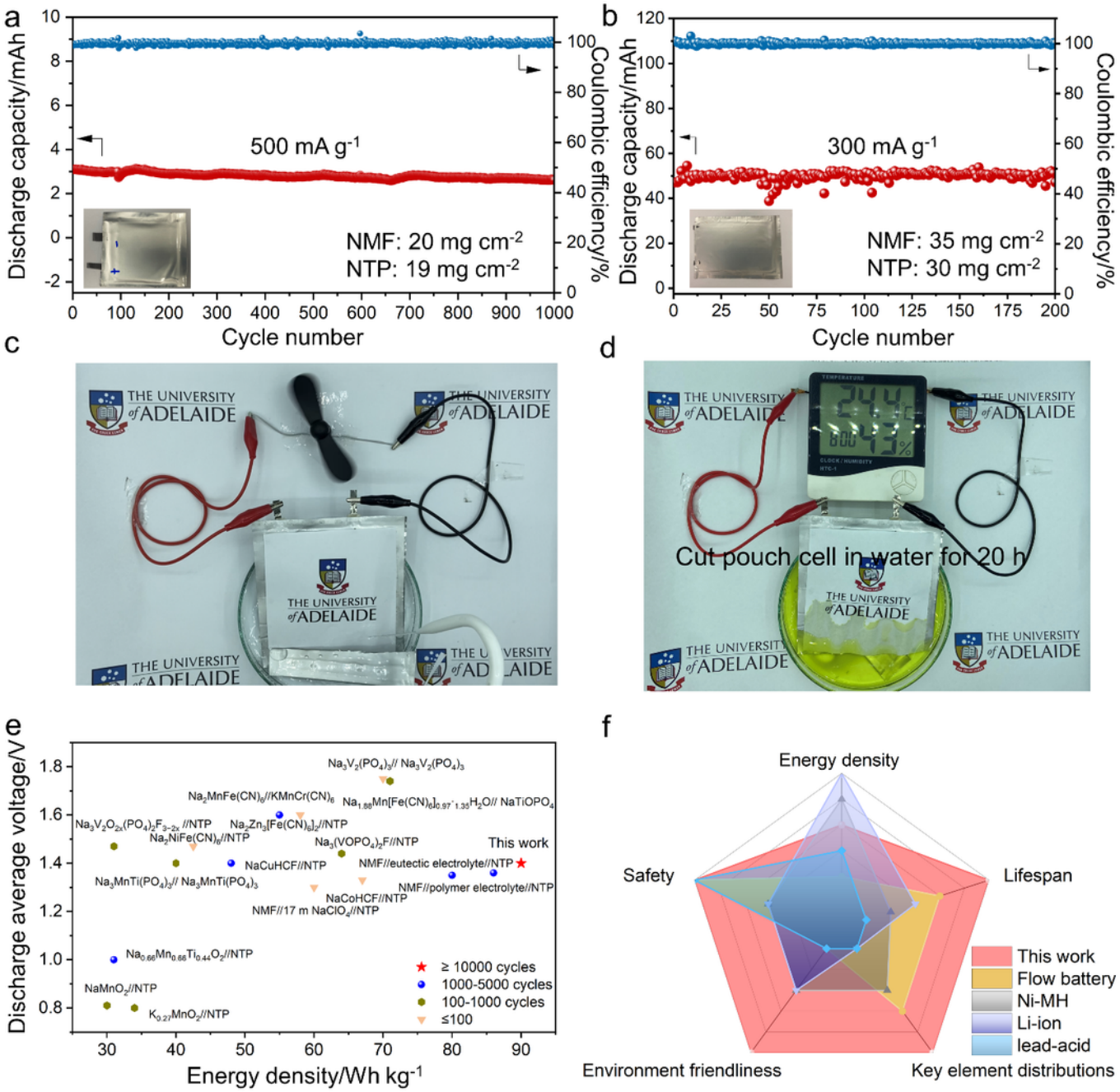

Figure 2

Electrochemical performance for NMF/NTP pouch cells and comparison with selected reports. a, Cycling performance for NMF/NTP pouch cell at a current density of 500 mA g^{-1}. b, Cycling performance for NMF/NTP pouch cell at 300 mA g^{-1}. c, Digital image of a cut pouch cell to power a fan in water. d, Digital image of a cut pouch cell to power a humidity clock in water. e, Comparison of lifespan and energy

density with reported aqueous Na-ion batteries. f, Comparison of present work with commercial batteries (as quantified in Supplementary Table 4).

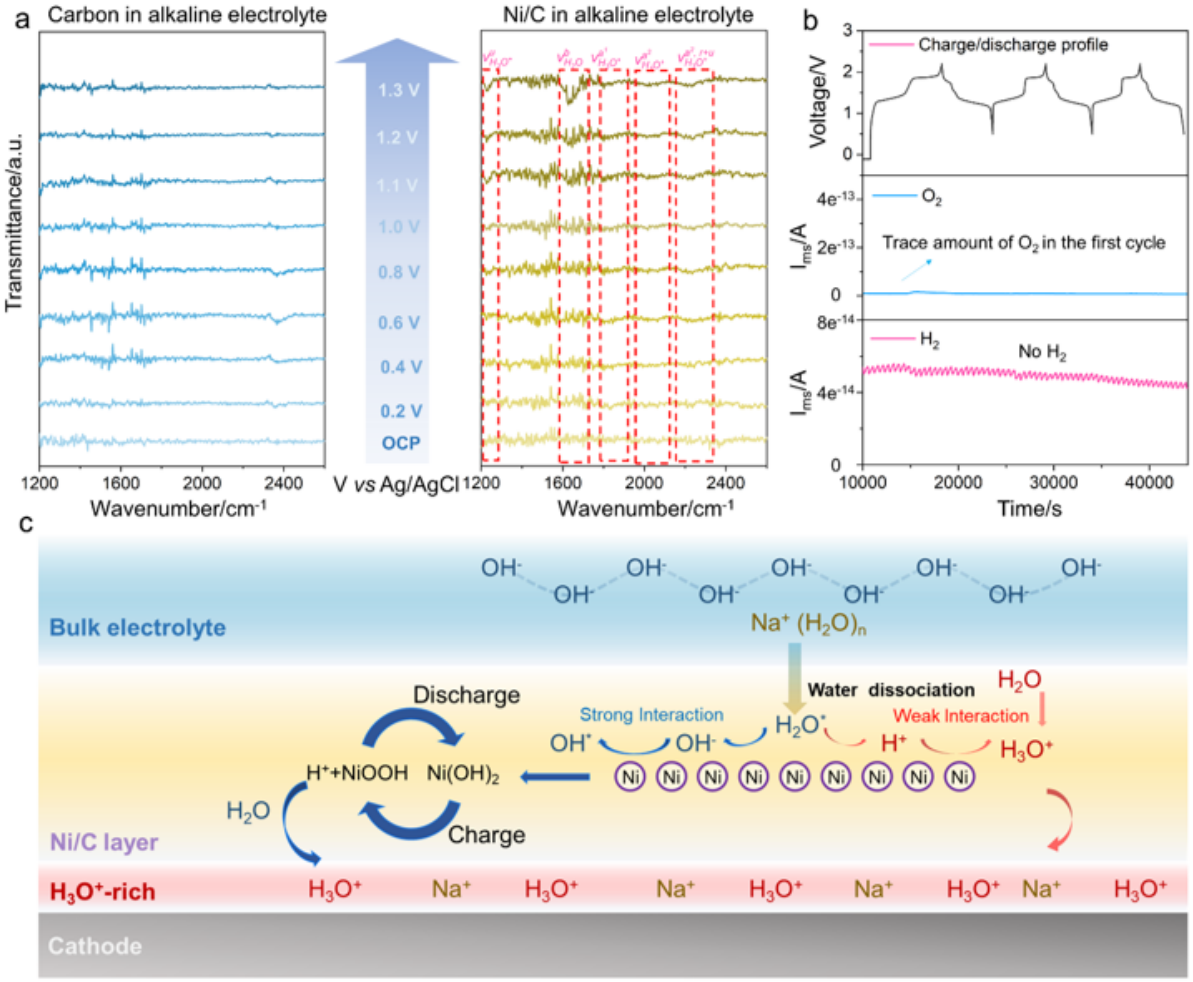

Fig. 3 | Generation of H_3O^+-rich micro-environment. a, *In-situ* surface-enhanced FTIR spectra for pure carbon and Ni/C at different potentials. Fundamental excitations of H_3O^+, denoted $\nu^{u}_{H_3O^+}$ (umbrella vibration), $\nu^{a^1}_{H_3O^+}$ (asymmetric O-H stretching), and resonance states between fundamental excitation of asymmetric O-H stretching and combination tones (r+u) denoted $\nu^{a^2,r+u}_{H_3O^+}$, where r and u represent, respectively, frustrated rotation and umbrella vibration. Bending of H_2O is denoted $\nu^{b}_{H_2O}$. **b**, *Operando* DEMS findings to determine H_2 and O_2 evolution during NMF/NTP battery cycling at 0.5 to 2.2 V at 0.5 C. **c,** Schematic for H_3O^+ accumulation mechanism on electrode surface coated with Ni/C in the alkaline electrolyte.

Figure 3

See image above for figure legend.

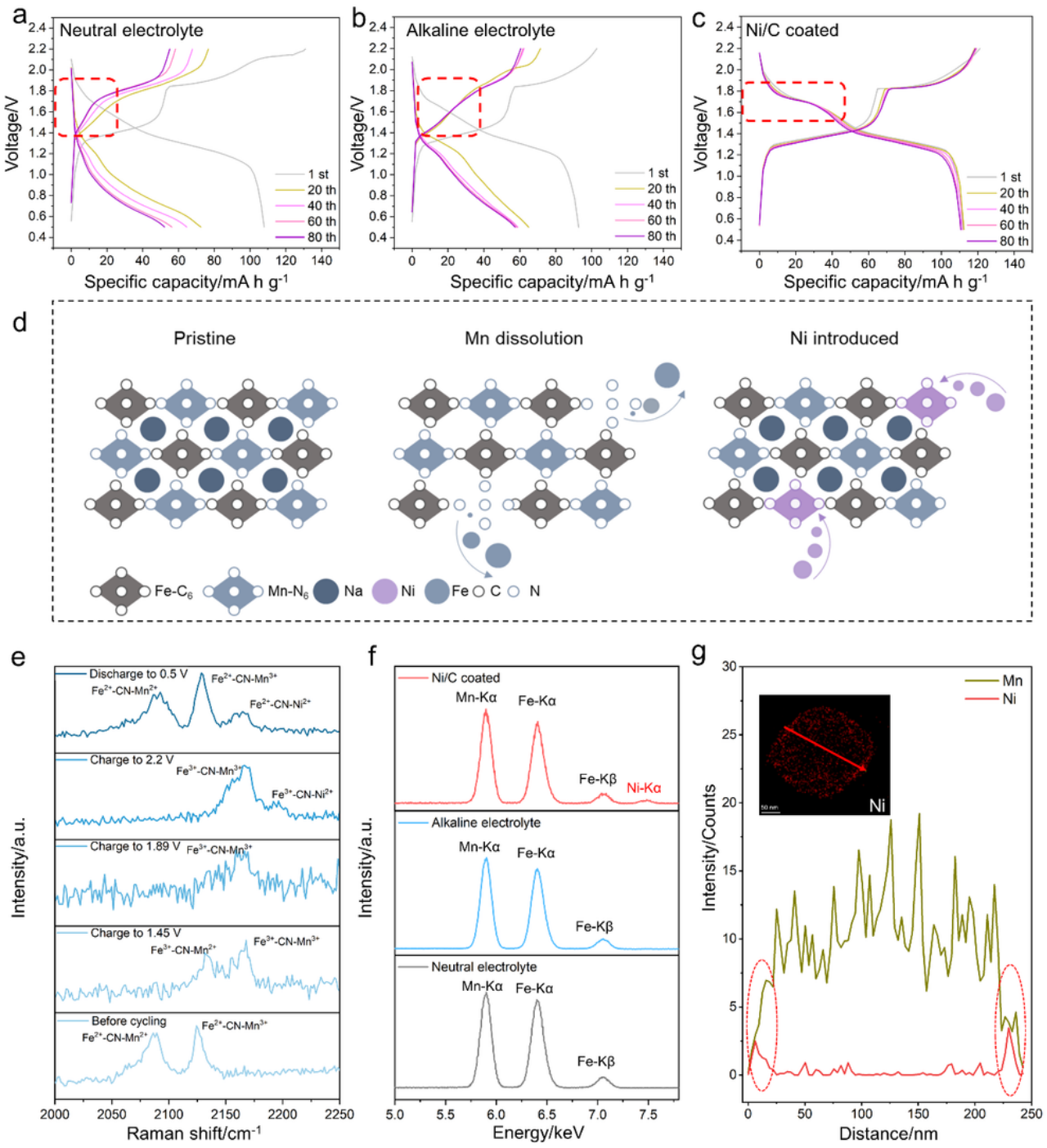

Figure 4

Determination of reaction mechanism(s) and *in-situ* Ni substitution. Charge/discharge curves for NMF/NTP cells in a, neutral electrolyte, b, alkaline electrolyte and c, alkaline electrolyte with Ni/C coating. d, Schematic for Ni/C coating for mitigating structural instability because of Mn dissolution in NMF cathdoe. e, *Operando* Raman spectra for Ni/C coated NMF cathode cycled in alkaline electrolyte. f, EDS spectra taken from NMF electrodes following cycling in neutral, alkaline electrolyte, and alkaline

electrolyte with Ni/C coating coating. g, STEM line scan for cycled NMF cathodes with Ni/C coating. Insets show Ni mapping for NMF.

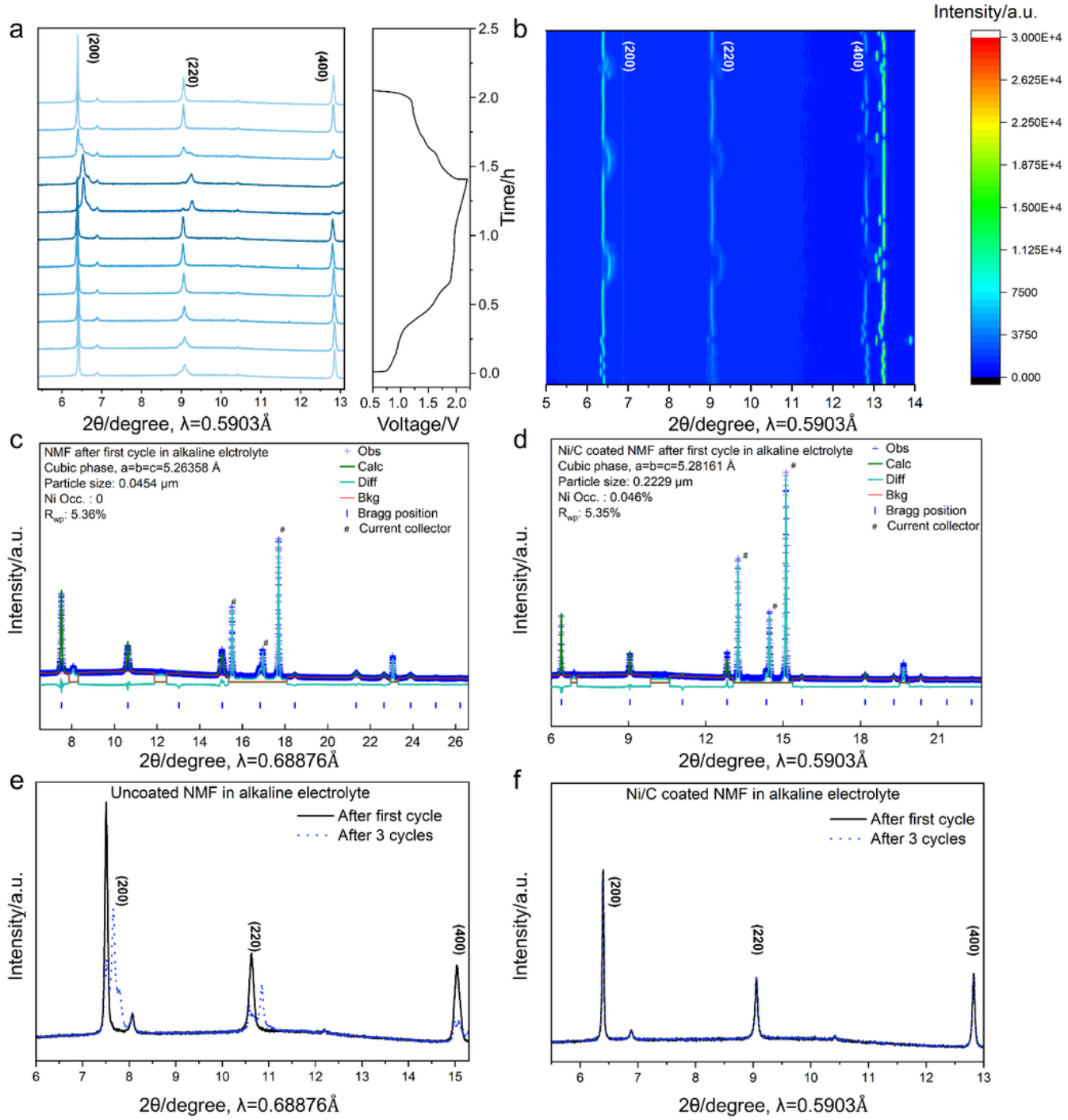

Figure 5

Operando structure analyses for NMF cathode during battery cycling at 0.5 to 2.2 V. a, (200), (220), and (400) reflections of synchrotron *operando* XRPD pattern. b, 2D contour plot for *operando* XRPD for the

first 3 cycles. Structural and Rietveld refinement of NMF cathode following 1st cycle in c, alkaline electrolyte and d, alkaline electrolyte with Ni/C coating. Comparison of XRPD pattern following 1st cycle and 3rd cycle in e, alkaline electrolyte and f, alkaline electrolyte with Ni/C coating.

Supplementary Files

This is a list of supplementary files associated with this preprint. Click to download.

- SupplementaryVideo1.mp4
- SupplementaryVideo2.mp4
- SupplementaryVideo3.mp4
- Supportinginformation.docx